Electronic Supplementary Information

Giant room-temperature barocaloric effect at the electronic phase transition in $Ni_{1-x}Fe_xS$

Jianchao Lin, Peng Tong,* Xuekai Zhang, Zichen Wang, Zhao Zhang, Bing Li,* Guohua Zhong,* Jie Chen, Yaoda Wu, Huaile Lu, Lunhua He, Bo Bai, Langsheng Ling, Wenhai Song, Zhidong Zhang and Yuping Sun

Experiment methods: Polycrystalline $Ni_{1-x}Fe_xS$ samples were prepared by a direct reaction of mixed elements in evacuated quartz tubes. Powders of Ni (3N), Fe (4N) and S (5N) were mixed in the desired ratio, grounded carefully, pressed in pellets, sealed in evacuated tubes (~10^{-4} Pa) and heated at 723 K for 3 days. The temperature was then slowly increased to 1223 K and annealed for another 5 days. After that, the tubes were quenched in ice water, the products were grounded, pressed into pellets, sealed in evacuated tubes, and then annealed at 973 K for a further 8 days, and finally quenched in ice water to obtain the homogeneous hexagonal-phase samples.

Room temperature (for all samples) and temperature dependent X-ray diffraction (for x=0.15 and 0.175) were measured on a Philips X'pert PRO X-ray diffractometer with Cu K_α radiations. Temperature dependence of thermal conductivity (κ-T) using a Thermal Transport Option (TTO) and specific heat were measured on a commercial Quantum Design Physical Property Measurement System (QD-PPMS). Magnetic susceptibility at ambient pressure was measured on a QD Superconducting Quantum Interference Device (QD-SQUID) magnetometer, on which pressure dependent magnetic susceptibility was carried out using the copper beryllium clamp type pressure cell.

Heat flow data were collected using a differential scanning calorimetry (μDSC 7 EVO, Setaram) at 0.1, 20, 40, 60, 80, and 100 MPa, respectively. The samples were capsuled in high-pressure cells and the applied pressures were accessed using a high-pressure gas panel that controls the pressure of nitrogen gas. Scanning rate is 2 K/minute for each measurement.

Temperature dependent Neutron powder diffraction experiments were performed between 5 K and 310 K on the time-of-flight diffractometer GPPD (the general purpose powder diffractometer) at CSNS (the China Spallation Neutron Source), Dongguan, China. Samples were loaded in 9.1 mm vanadium cans and patterns were collected with wavelength band (0.1-4.9 Å).

Theoretical calculation method: Within the framework of density functional theory, the Vienna ab initio simulation package (VASP) based on the projector augmented wave method was employed to investigate the phase transitions. In this calculation, computational parameters are referred to previous study.[1] The generalized gradient approximation (GGA) of the exchange correlation functional (Perdew-Burke-Ernzerh of 96, PBE) was adopted. And GGA+U method was used to consider the electronic correlation effects. The U values were set as 2.5 eV for Ni and 4.0 eV for Fe, respectively, to reproduce the experimental band-gap. An energy cutoff of 350 eV was adopted. Structural optimization used a conjugate-gradient algorithm, and the k-point of the Brillouin zone was a 0.04 $Å^{-1}$ interval distribution of Monkhorst-Pack. The k-point interval of the total energy self-consistent calculation was 0.02 $Å^{-1}$. The energy convergence standard was 10^{-6} eV. The convergence criterion of the force was 10^{-3} eV/Å.

Supplementary figures and captions:

Fig. S1 Entropy change at T_t at ambient pressure for $Ni_{1-x}Fe_xS$. (a) Calorimetric heat flow (dQ/dT) curves measured on heating and cooling. (b) Transition temperature T_t and the related entropy change ΔS_t derived from the dQ/dT curves. The open and solid circles represent the entropy change from the cooling and heating processes, respectively.

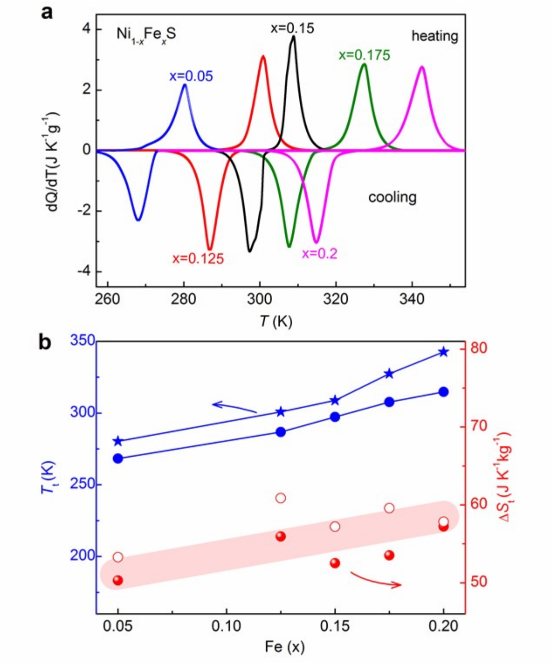

Fig. S2 Barocaloric effect for $Ni_{1-x}Fe_xS$ on heating. (a)-(d) The dQ/dT curves measured on heating at different pressures. (e)-(h) Entropy change (ΔS_p) purely due to the phase transition at T_t under various pressures. The compositions are marked in each panel.

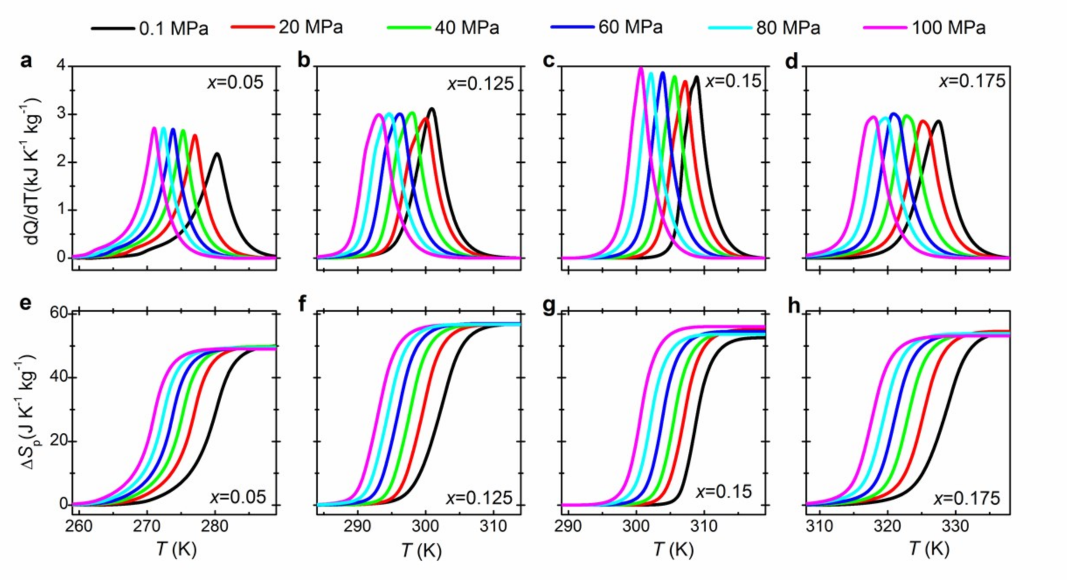

Fig. S3 Barocaloric effect for $Ni_{1-x}Fe_xS$ (x = 0.15) on both cooling and heating runs. (a) dQ/dT curves measured at different pressures. (b) Entropy change (ΔS_p) purely due to the phase transition at T_t with the application of various pressures. (c) Pressure induced entropy change (ΔS_{BC}) as a function of temperature relative to the ambient case.

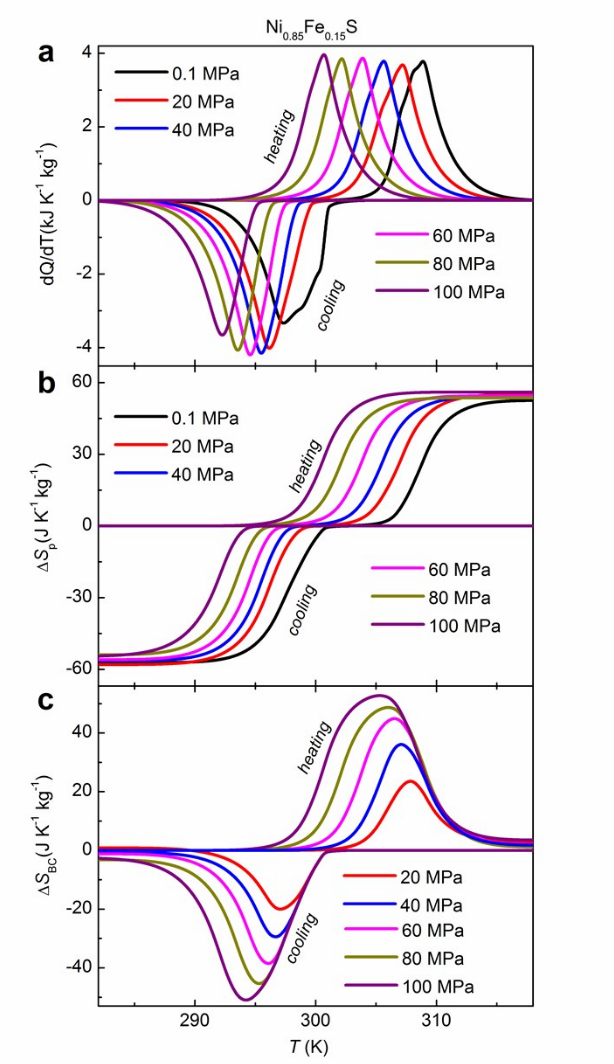

Fig. S4 Thermal conductivity k(T) for $Ni_{1-x}Fe_xS$.

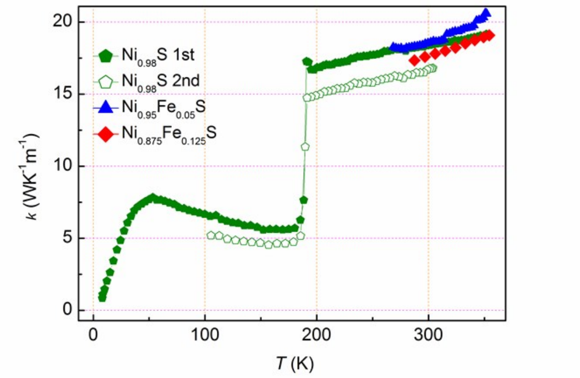

For $x > 0.125$, the structural transition with a large volume change is near or above room temperature. So, microcracks naturally exist as those samples experienced the structural transition when quenched into water during the preparation process. Consequently, thermal conductivity for those samples cannot be accurately measured using the TTO equipped in the QD-PPMS. Instead, only the data above T_t is recorded for $x = 0.05$, 0.125. As a reference, k(T) for $Ni_{0.98}S$ with much smaller volume change at T_t (190 K) was measured. In the high-temperature metallic state, k(T) recorded in the first run is close to those of $x = 0.05$, 0.125. However, the data both above and below T_t are remarkably reduced in the second run as a result of transition induced microcracks.

Fig. S5 Temperature dependent magnetization *M*(T) under 0.1 MPa, 250 MPa, 500 MPa, and 1000 MPa. The samples were also inserted in the same pressure cell for measurement at 0.1 Mpa. (a) *M*(T) under field-cooled-cooling (FCC) and field-cooled-warming (FCW) modes for *x* = 0. (b) *M*(T) under FCC and FCW modes for *x* = 0.05. (c) *M*(T) under FCC and FCW modes for *x* = 0.175. (d) *M*(H) measured at 5 K directly without inserting the sample in pressure cell for x = 0, 0.05 and 0.175. The measurement magnetic fields are marked in (a)-(c).

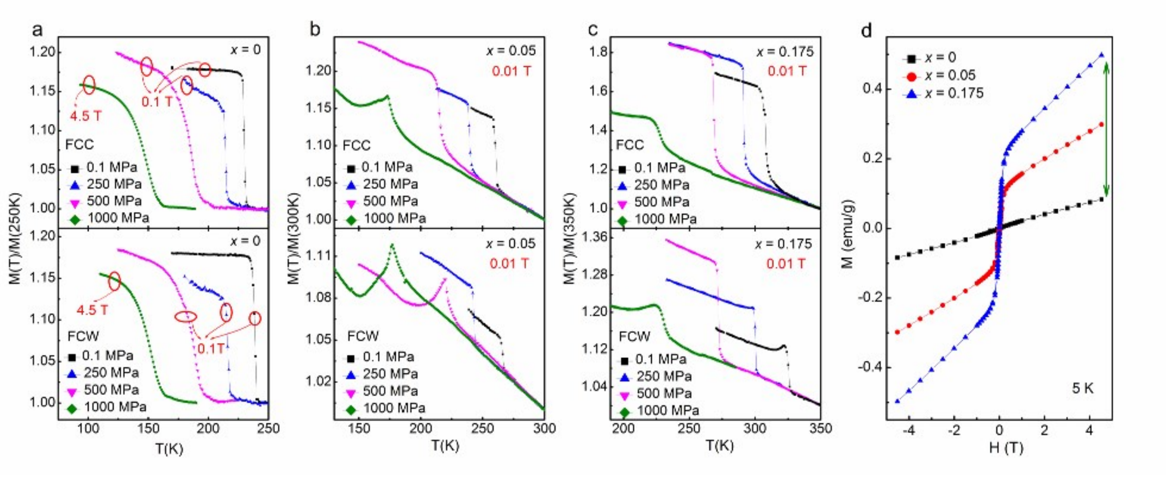

As shown in Fig. S5d, for x = 0, *M*(H) at 5 K shows a typical AFM behavior (*M* is linearly dependent on H). But for x > 0 there is a clear deviation from the AFM behavior, indicating a FM-like order component coexisting with the dominant AFM one. The arrow in Fig. S5d indicates the contribution from the FM-like component to the total magnetization. Such extra magnetization is only 0.49 emu/g even at 4.5 T, corresponding to 0.008 μ_B/Ni(Fe). This moment is too small to be detected by neutron powder diffractions (Fig. S6-S7).

Fig. S6 Temperature dependent neutron powder diffractions (NPD) and X-ray diffractions (XRD) for $Ni_{1-x}Fe_xS$. (a) Temperature dependent NPDs for for *x* = 0.05. (b) Temperature dependent NPDs for for *x* = 0.125. (c) Temperature dependent XRDs for *x* = 0.15. (d) Temperature dependent XRDs for *x* = 0.175. Muller indexes are shown in each panel. The detailed fitting results of the NPD and XRD patterns can be found in Table S2 and Table S3, respectively.

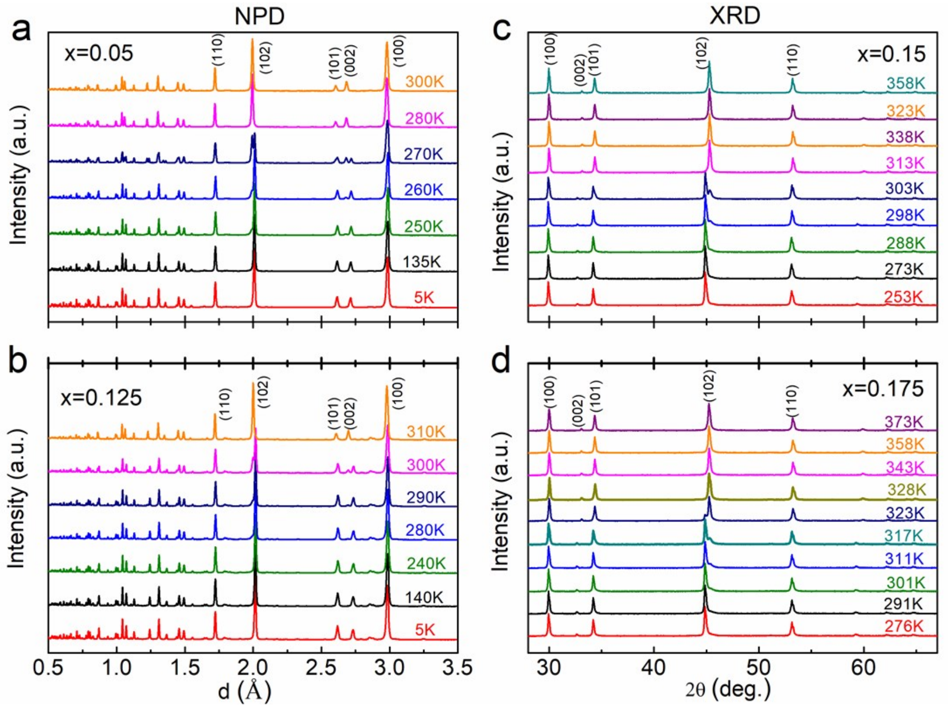

When the measurement temperatures are within the temperature range of phase transition, both the low-temperature (LT) and high-temperature (HT) phases coexist, as evidenced by the splitting of (002) peak (e.g., the pattern at 270 K for *x* = 0.05). In the NPD patterns when temperature is decreased to below the antiferromagnetic (AFM) to paramagnetic transition, magnetic scattering shows up and makes the some nuclear diffractions stronger. For instance, the intensity of (101) in clearly enhanced at low temperatures for both *x* = 0.05 and 0.125.

Fig. S7 Typical Rietveld refinements of powder neutron diffraction data for $Ni_{1-x}Fe_xS$ with $x = 0.05$ using GSAS-II program.[2] (a) at 300 K. (b) at 270 K. (c) at 5 K. The experimental (exp), calculated (cal) patterns and the difference between them (diff) are plotted. The vertical bars show the Bragg peak positions. The AFM structure is shown in the inset of (c). The goodness of fit is shown in Table S3.

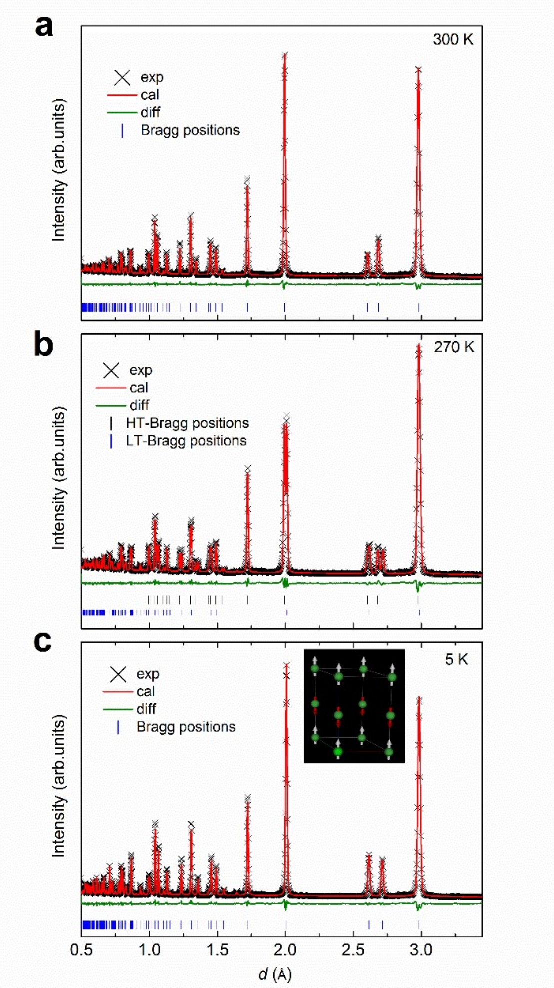

At 270 K, both the LT and HT phases coexist. The AFM diffractions show up at 5 K and also in the LT phase of 270 K data. Because the magnetic and lattice diffractions share the same Bragg positions for the present AFM configuration, their positions are not specially marked. The AFM structure is as same as that of NiS,[3] namely, the moments are coupled ferromagnetically in the hexagonal layers and point along c direction, while antiferromagnetically coupled between adjacent layers (See inset of Fig. S7c). In other words, the AFM structure has the same period as that of nuclear crystal structure. Within the resolution of our NPD data, we didn't detect the existence of any magnetic orders other than the AFM one.

Fig. S8 Specific heat for *x* = 0.05 and 0.15.

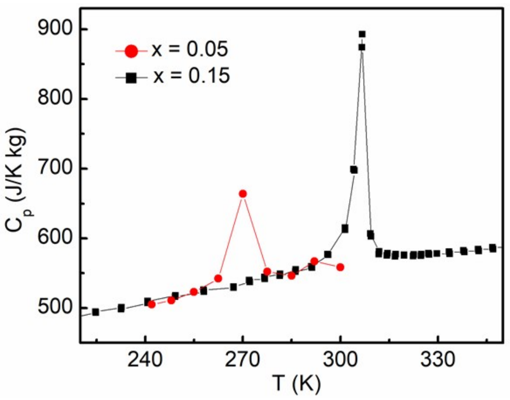

Fig. S9 The entropy change curves under both ambient and 100 MPa for *x* = 0.05 considering **(a)** and without considering the heat capacity **(b)**. **(c)** The pressure driven entropy change before and after considering the specific heat for *x* = 0.05. **(d)** The dependence of adiabatic temperature change on the entropy change based on the Fig. S9a and Fig. S9b.

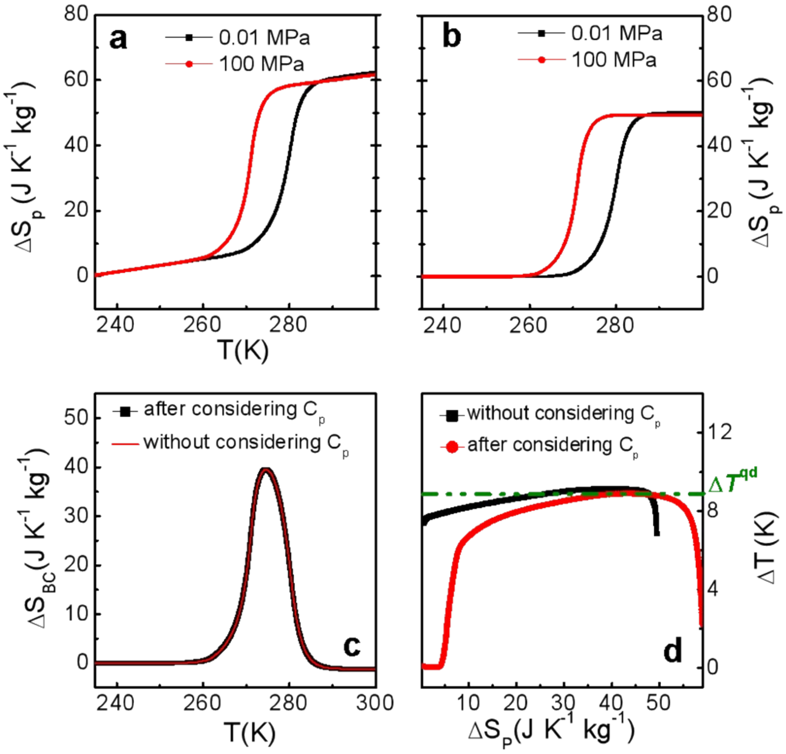

The temperature dependent entropy at pressure p, *S*(T,p) can be calculated by using,

$$S(T,p)=\int_{T_0}^{T}\frac{C^L}{T}dT \text{ for } T \le T_1 \qquad (1)$$

$$S(T,p) = S(T_1,p) + \int_{T_1}^{T} \frac{1}{T}(C + dQ/dT)dT \text{ for } T_1 \le T \le T_2 \tag{2}$$

$$S(T,p) = S(T_2,p) + \int_{T_2}^{T} \frac{C^H}{T}dT \text{ for } T \ge T_2. \tag{3}$$

Here $dQ/dT = \dot{Q}/\dot{T}$ with $\dot{Q}$ being the heat flux measured by DSC and $\dot{T}$, the heating rate. C^L and C^H represent for the specific heat below and above the phase transition range, respectively. $C = xC^L + (1-x)C^H$ where x is the fraction of the low-temperature phase in the phase transition region, which was determined by NPD.

As shown in Fig. S9a, if considering the specific heat, the calculated entropy change at both ambient and 100 MPa have a tiny slope compared with the curves without taking into account the specific heat (Fig. S9b). As shown in Fig. S9c, the pressure-induced isothermal entropy changes in the vicinity of phase transition after considering specific heat are consistent no matter the heat capacity was considered or not. Based on the dependence of temperature on the entropy change, the adiabatic temperature change was calculated and shown in Fig. S9d. It is clear that the maximum ΔT^{qd} is not influenced by considering the specific heat in the entropy curves.

Fig. S10 Calculated total and projected density of states (DOS) and band structures along high k-point paths for $Ni_{0.75}Fe_{0.25}S$ at different pressures, based on GGA+*U* method. (a) at 0 GPa; (b) at 0.5 GPa.

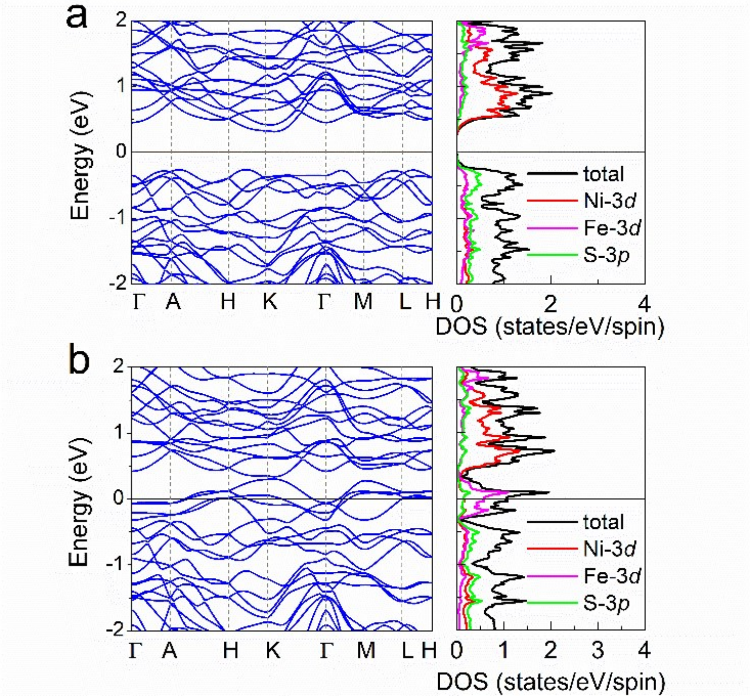

Fig. S11 Calculated total density of states (DOS) for $Ni_{15}S_{16}$ (namely with 1/16 Ni vacancies) at different pressures, based on GGA+*U* method.

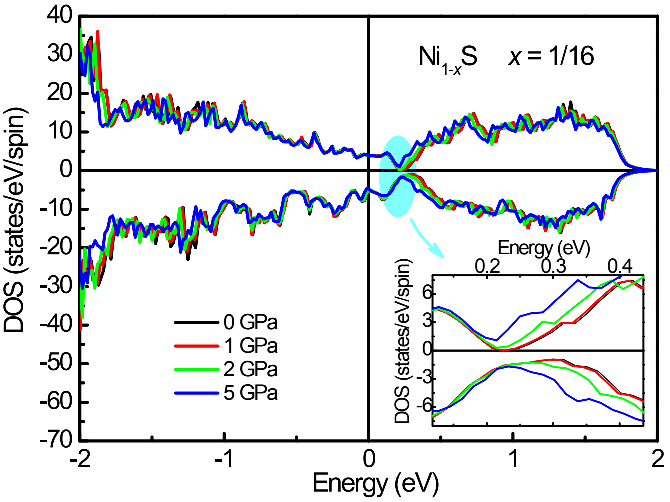

The experimentally observed critical pressure (2 GPa) of nonmetal-metal transition corresponds to a sample with Ni deficiencies.[4] That sample's transition temperature (T_t ~ 210 K) is smaller than the sample without Ni deficiencies (T_t ~ 260 K). As reported,[4] the critical pressure is decreased with increasing Ni vacancies. So, the Ni vacancy plays an important role in determining the critical pressure. In order to reduce the computation time, compound with 6.25% Ni vacancies ($Ni_{15}S_{16}$) was selected for calculation. The result indicates a metallic ground state, in good agreement with the experimental result that the metal-nonmetal transition is absent when the vacancies are larger than 4%. As shown in inset of supplementary Fig. S10, DOS increases with increasing pressure and finally the energy gap is closed above 1 GPa for $Ni_{15}S_{16}$. Such a critical pressure is much suppressed compared with the one (10 GPa) for stoichiometric NiS compound.

Supplementary Tables

Table S1. A comparison of transition temperature (T_t), entropy change (ΔS_{BC}) at 100 MPa, thermal conductivity (k) for the reported giant BC materials and $Ni_{0.85}Fe_{0.15}S$. For the intermetallic compounds, the k values just before and after the phase transiion are averaged and used for comparison. As to $GaNMn_3$, $MnCoGeB_{0.03}$ and [TPrA][Mn(dca)$_3$], k values are not available in the literatures, so those from similar compositions are listed. k values for $Fe_{49}Rh_{51}$, $(Ni_{50}Mn_{31.5}Ti_{18.5})_{99.8}B_{0.2}$ are calculated based on Wiedemann-Franz law by using the resistivity data from the cited references. The values not referenced are from the Ref. 5.

compound	T_t (K)	ΔS_{BC} (J kg^{-1} K^{-1})	ΔS_{BC} (J cm^{-3} K^{-1})	k (W K^{-1} m^{-1})
$Fe_{49}Rh_{51}$	310	12	0.118	7.1 [11]
$LaFe_{11.33}Co_{0.47}Si_{1.2}$	250	5.5	0.039	7[12]
$Gd_5Si_2Ge_2$	260	9	0.068	5.64[12]
$GaNMn_3$	290	21	0.146	6.5[13]
$NiNMn_3$	262	21[6]	0.144[6]	-
$Ni_{51}Mn_{33}In_{16}$	330	17.5	0.143	8[14]
$(Ni_{50}Mn_{31.5}Ti_{18.5})_{99.8}B_{0.2}$	255	30[7]	0.211[7]	3.95[15]
$MnCoGeB_{0.03}$	286	35[8]	0.28[8]	6.4[16]
$(MnNiSi)_{0.62}(FeCoGe)_{0.38}$	338	43.6	0.318	-
AgI	390	61[8]	0.35[8]	0.2[17]
$(NH_4)_2SO_4$	220	60	0.106	0.82[18]
$(NH_4)_2SnF_6$	110	61	0.175	-
[FeL$_2$][BF$_4$]$_2$	262	68[9]	0.107[9]	-
[TPrA][Mn(dca)$_3$]	330	26.5[8]	0.035[8]	1.4[19]
NPG	313	400[10]	0.425[10]	0.12[20]
$Ni_{0.85}Fe_{0.15}S$ (this work)	303	52.8	0.285	11.5

Table S2. The fitting results of XRD patterns at different temperature for x = 0.15 and x = 0.175 using Rietica program. In the P6$_3$/mmc crystal structure, Ni/Fe locates at (0, 0, 0), and S locates at (1/3, 2/3, 1/4) positions. a_L and c_L indicate the lattice parameters of the low-temperature phase; a_H and c_H indicate the lattice parameters of the high-temperature phase; P_L indicates the content of low-temperature phase; R_p, R_{wp} and χ^2 are the reliability factors which determine the quality of Rietica refinement (R_p : the profile R-factor; R_{wp} : the weighted R_p; χ^2: the goodness of fit).

The fitting results of XRD patterns for x = 0.15

T (K)	a_L (Å)	c_L (Å)	a_H (Å)	c_H (Å)	P_L	R_p	R_{wp}	χ^2
358	——	——	3.4445(2)	5.4113(3)	0	2.36	3.47	5.29
338	——	—	3.4442(2)	5.4103(3)	0	2.42	3.56	5.63
323	——	——	3.4424(2)	5.4094(2)	0	2.46	3.62	5.82
313	——	——	3.4416(2)	5.4082(3)	0	2.45	3.57	5.68
303	3.4464(2)	5.4773(3)	3.4391(4)	5.3994(6)	0.802	1.92	2.78	3.49
298	3.4510(2)	5.4796(3)	3.4390(5)	5.3840(9)	0.902	1.93	2.68	3.24
288	3.4506(2)	5.4794(3)	3.4388(4)	5.3827(7)	0.950	2.03	2.74	3.37
273	3.4510(2)	5.4808(3)	3.4388(4)	5.3824(4)	0.961	1.97	2.62	3.08
253	3.4486(2)	5.4784(3)	3.4378(3)	5.3811(4)	0.970	2.06	2.76	3.44

The fitting results of XRD patterns for x = 0.175

T (K)	a_L (Å)	c_L (Å)	a_H (Å)	c_H (Å)	P_L	R_p	R_{wp}	χ^2
373	——	——	3.4405(2)	5.4156(3)	0	2.23	3.07	4.19
358	——	——	3.4400(1)	5.4146(3)	0	2.27	3.28	4.76
343	——	——	3.4395(1)	5.4139(2)	0	2.32	3.36	4.96
328	——	——	3.4391(1)	5.4132(2)	0	2.29	3.31	4.53
323	3.4467(3)	5.4965(4)	3.4439(8)	5.4211(9)	0.191	2.27	3.13	4.43
317	3.4482(2)	5.4877(3)	3.4405(5)	5.4071(9)	0.847	1.95	2.68	3.24
311	3.4485(2)	5.4886(3)	3.4416(7)	5.4138(8)	0.897	2.17	2.97	3.94
301	3.4482(1)	5.4884(2)	3.4428(7)	5.4199(9)	0.924	1.92	2.59	3.04
291	3.4480(2)	5.4883(4)	3.4430(4)	5.4261(3)	0.950	2.36	3.27	4.76

Table S3. The fitting results of NPD patterns at different temperature for *x* = 0.05 and *x* = 0.125 using GSAS-II program. a_L and c_L indicate the lattice parameters of the low-temperature phase; a_H and c_H indicate the lattice parameters of the high-temperature phase; P_L indicates the content of low-temperature phase; wR and GOF are the reliability factors which determine the quality of fitting (wR: weighted residual for powder diffraction; GOF: the goodness of fit). The other fitting results can be found in CIF files uploaded.

The fitting results of NPD patterns for *x* = 0.05

T (K)	a_L (Å)	c_L (Å)	a_H (Å)	c_H (Å)	Magnetic moment (μ_B)	P_L	wR	GOF
300	— —	— —	3.4405(1)	5.3696(1)	0	0	6.871%	2.97
280	— —	— —	3.4396(1)	5.3673(1)	0	0	7.19%	3.11
270	3.4490(1)	5.4373(1)	3.4387(1)	5.3622(1)	1.31(2)	0.499	7.76%	3.38
260	3.4493(1)	5.4361(1)	3.4318(1)	5.3588(1)	1.31(2)	0.860	7.65%	3.33
250	3.4491(1)	5.4358(1)	3.4279(1)	5.3588(1)	1.34(2)	0.909	7.06%	3.07
135	3.4468(1)	5.4304(1)	— —	— —	1.42(2)	1	7.81%	3.40
5	3.4459(1)	5.4276(1)	— —	— —	1.45(2)	1	7.93%	4.77

The fitting results of NPD patterns for *x* = 0.125

T (K)	a_L (Å)	c_L (Å)	a_H (Å)	c_H (Å)	Magnetic moment (μ_B)	P_L	wR	GOF
310	— —	— —	3.4403(1)	5.3967(2)	0	0	10.49%	4.63
300	3.4451(3)	5.4632(2)	3.4354(5)	5.3846(5)	1.39(2)	0.854	10.53%	4.91
290	3.4491(3)	5.4687(2)	3.4318(5)	5.3886(5)	1.51(2)	0.918	14.98%	6.96
280	3.4485(2)	5.4689(2)	— —	— —	1.55(3)	1	14.12%	5.93
240	3.4480(1)	5.4683(2)	— —	— —	1.62(2)	1	12.33%	5.74
140	3.4461(1)	5.4645(2)	— —	— —	1.69(2)	1	12.87%	6.02
5	3.4452(1)	5.4620(2)	— —	— —	1.73(3)	1	11.51%	5.64

References

1 Q. Liu, G. H. Zhong, F. F. Ming, K. D. Wang and X. D. Xiao, *Phys. Rev. B*. 2015, **91**, 155417.

2 B. H. Toby and R. B. V. Dreele, *J. Appl. Crystallogr.,* 2013, **46**, 544-549.

3 J. T. Sparks and T. Komoto, *J. Appl. Phys.,* 1963, **34**, 1191.

4 D. B. McWhan, M. Marezio, J. P. Remeika and P. D. Dernier, *Phys. Rev. B,* 1972, **5**, 2552.

5 L. Mañosa and A. Planes, *Adv. Mater.,* 2017, **29**, 1603607.

6 D. Boldrin, E. Mendive-Tapia, J. Zemen, J. B. Staunton, T. Hansen, A. Aznar, J.-L. Tamarit, M. Barrio, P. Lloveras, J. Kim, X. Moya and L. F. Cohen, *Phys. Rev. X,* 2018, **8**, 041035.

7 A. Aznar, A. G.-Condal, A. Planes, P. Lloveras, M. Barrio, J. -L. Tamarit, W. X. Xiong, D. Y. Cong, C. Popescu and L. Mañosa, *Phys. Rev. Mater.,* 2019, **3**, 044406.

8 A. Aznar, P. Lloveras, J.-Y. Kim, E. S. Taulats, M. Barrio, J. L. Tamarit, C. F. S.-Valdés, J. L. S. Llamazares, N. D. Mathur and X. Moya, *Adv. Mater.,* 2019, **31**, 1903577.

9 S. P. Vallone, A. N. Tantillo, A. M. dos Santos, J. J. Molaison, R. Kulmaczewski, A. Chapoy, P. Ahmadi, M. A. Halcrow and K. G. Sandeman, *Adv. Mater.,* 2019, **31**, 1807334.

10 B. Li, Y. Kawakita, S. O.-Kawamura, T. Sugahara, H. Wang, J. F. Wang, Y. N. Chen, S. I. Kawaguchi, S. Kawaguchi, K. Ohara, K. Li, D. H. Yu, R. Mole, T. Hattori, T. Kikuchi, S.-i. Yano Z. Zhang, Z. Zhang, W. J. Ren, S. C. Lin, O. Sakata, K. Nakajima and Z. D. Zhang, *Nature,* 2019, **567**, 506.

11 C. J. Schinkel, R. Hartog and F. H. A. M. Hochistenbach, J. Phys. F: Met. Phys., 1974, **4**, 1412.

12 S. Fujieda, Y. Hasegawa, A. Fujita, and K. Fukamichi, *J. Appl. Phys.,* 2014, **95**, 2429.

13 J. C. Lin, B. S. Wang, P. Tong, W. J. Lu, L. Zhang, X. B. Zhu, Z. R. Yang, W. H. Song, J. M. Dai and Y. P. Sun, *Appl. Phys. Lett.,* 2011, **98**, 092507.⍰

14 B. Zhang and X. X. Zhang, S. Y. Yu, J. L. Chen, Z. X. Cao and G. H. Wu, *Appl. Phys. Lett.,* 2007, **91**, 012510.

15 E. S. Belosludtseva, N. N. Kuranova, N. I. Kourov, V. G. Pushin and A. N. Uksusnikov, *Tech. Phys.,* 2015, **60**, 1330.

16 F. Zhu, J. C. Lin, W. B. Jiang, C. Yang, L. F. Li, X. K. Zhang, W. H. Song, X. B. Zhu, P. Tong and Y. P. Sun, *Scr. Mater.,* 2018, **150**, 96.

17 M. C. Goetz and J. A. Cowen, *Solid State Comm.,* 1982, **41**, 293.

18 T. K. Song , S.-M. Lee , Y. S. Yu and S.-I. Kwun, *Ferroelectrics,* 1994, **159**, 215.

19 W. D. C. B. Gunatilleke, K. Wei, Z. Niu, L. Wojtas, G. Nolas and S. Q. Ma, *Dalton Trans.,* 2017, **46**, 13342.

20 B. Praveen and S. Suresh, *Eng. Sci. Technol. Int. J.,* 2018, **21**, 1086.